Uniformly Distributed Circular Porous Pattern Generation On Surface For 3D Printing

Sungha Yoon[1], Chaeyoung Lee[1], Jintae Park[1], Darae Jeong[2]
and Junseok Kim[1],*

[1] *Department of Mathematics, Korea University, Seoul 02841,
Republic of Korea*
[2] *Department of Mathematics, Kangwon National University,
Gangwon-do 24341, Republic of Korea*

Abstract. We present an algorithm for uniformly distributed circular porous pattern generation on surface for three-dimensional (3D) printing using a phase-field model. The algorithm is based on the narrow band domain method for the nonlocal Cahn–Hilliard (CH) equation on surfaces. Surfaces are embedded in 3D grid and the narrow band domain is defined as the neighborhood of surface. It allows one can perform numerical computation using the standard discrete Laplacian in 3D instead of the discrete surface Laplacian. For complex surfaces, we reconstruct them from point cloud data and represent them as the zero-level set of their discrete signed distance functions. Using the proposed algorithm, we can generate uniformly distributed circular porous patterns on surfaces in 3D and print the resulting 3D models. Furthermore, we provide the test of accuracy and energy stability of the proposed method.

1. Introduction

Three-dimensional (3D) surface models have been studied with great interest in various fields. For this reason, design, synthesis, deformation, and transformation on surface mesh for 3D fabrication have been studied [7, 27, 30]. Typically, 3D printing technology is used in medical fields. Because making 3D models should be not only

---

economic but also hygiene in medical field applications, additional remeshing methods are required. Likewise, additive manufacturing techniques such as representation and optimization are also important for printing actual 3D models [3, 14, 28, 33]. In particular, 3D surface with porous pattern is a representative example of complex structures [16]. Having porosity has many advantages in various fields: biomaterial, tissue engineering, and clinical medicine, etc. However, a large amount of data is required to represent such complex shapes, which requires more computational time. For this reason, it is important to remesh the surface of 3D model. There are various strategies to remesh surfaces. The authors in [40] used an electrospinning and 3D printing technology to fabricate a 3D composite structure. The authors in [26] showed a durable superhydrophobic porous surface can be used to separate two fluids, oil and water, using a 3D printing. Jakus *et al.* [17] introduced a procedure using extending 3D printing technology and traditional salt-leaching to make 3D print materials and structures with high porosity. These methods used 3D printing technology, however, only created basic surfaces or structures, and it was difficult to apply it on complex surfaces. Another widely used example of creating porous surface is the Voronoi diagram. Pellerin *et al.* [29] and Valette *et al.* [36] used a remeshing method based on the Voronoi diagrams with the finite element method. Chaidee *et al.* [6] generated spherical Laguerre Voronoi diagrams for approximating spherical polygonal tessellations. In [2], the authors presented a surface modification method to make 3D models which are shaped with Voronoi and fractal diagram surface. In medical manufacturing field, to make a comfortable and aesthetically orthopedic casts for patients without sacrificing any of its functionality, a funnel-shaped cast model was proposed in [25] and it can create smooth edges to prevent bruises from movements of injured limbs. Furthermore, different structures of orthopedic casts such as non-uniform Voronoi, regular cell, mesh edges pattern were designed on the surface by different technical methods. In [13], the authors proposed a low-cost 3D scanning and used computer-aided design (CAD) software to generate different structures of orthopedic casts as shown in Fig. 1.
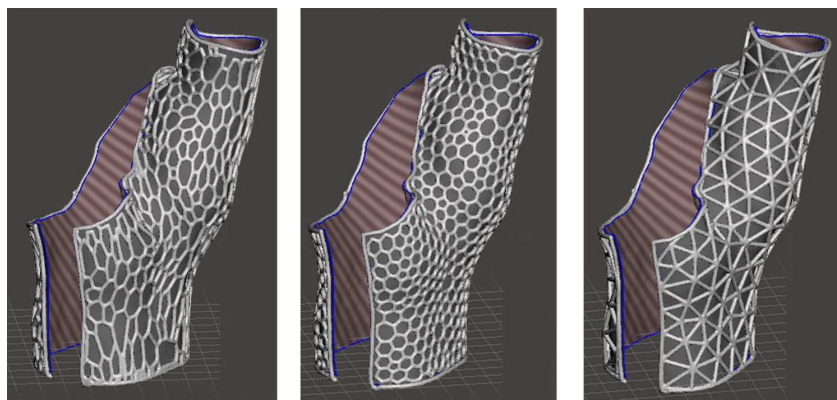

Figure 1: Different structures by using Autodesk Meshmixer free software. Reprinted from Fernandez-Vicente et al. [13] with permission from Rapid Prototyping Journal.

The authors in [34] developed a mapping algorithm to generate Voronoi-based composite structures.

Meanwhile, 3D printing using classical Voronoi type tessellation has a limitation on the generation of uniform distribution of porosity and shape of holes on a surface. For example, surfaces with small curvature have large holes because they have a small number of the vertex points, hence it may cause durability problem in 3D printing models. To address this problem, Wang *et al.* [37] presented two intrinsic techniques for calculating centroidal Voronoi tessellation (CVT) on triangle meshes. The authors adopted the Lloyd and the L-BFGS frameworks with the discrete exponential map to calculate the Riemannian center and the center of mass for any geodesic Voronoi diagram. These methods imply the independence of working spaces and are suitable for arbitrary topology and geometry, hence they overcome shortcomings of the extrinsic approaches. Furthermore, Zhang *et al.* [41] proposed the blue-noise sampling under capacity constraints. Compared to the conventional method using Poisson disk sampling with blue-noise properties [11], this method allows more precise capacity limitation by applying restricted power tessellation on surfaces; hence quadratic errors with respect to the capacities are much smaller. Recently, Schumacher *et al.* [31] proposed the example-based method for stencil patterns which are evaluated by energy minimizing optimization problems. This method has merit of being structurally sound and quick to create patterns, moreover, patterns can be customized as designers want to.

Unlike the methods described above, however, it is possible to fabricate surfaces with uniformly distributed circular porous pattern regardless of curvature restriction using the partial differential equations. As one of the major prior studies, Turk [35] presented a method generating textures using reaction-diffusion to fit the geometry of arbitrary polyhedral surfaces. The paper contained mesh construction and rendering process for 3D objects. Because the method is directly applied to the surface mesh itself, it has an advantage that the shape of patterns does not change significantly depending on geometry of surfaces. In a related study, Jeong and Kim [18] investigated various patterns on surfaces using the nonlocal Cahn–Hilliard (CH) equation for diblock copolymers in the field of materials science. The authors used the simple closest point method with the pseudo-Neumann boundary condition and the narrow band domain to simulate patterns on curved surfaces. In phase-field models, the CH equation has been widely investigated. The CH equation was developed for modeling the spinodal decomposition and coarsening dynamics in binary alloys [5], which is a H^{-1} gradient flow from the Ginzburg–Landau free energy functional. It has been investigated numerically [10, 23] and also has been applied in various fields such as image segmentation [24], image inpainting [4, 8], multiphase flows [15], formation of quantum dots [38]. Furthermore, many researchers have studied the CH type equations [20, 39, 42] for pattern formation by using coarsening dynamics. The main purpose of this paper is to use the nonlocal CH equation to generate uniformly distributed circular porous pattern on simple and complex surfaces for 3D printing. We perform the test of accuracy and energy stability of the method. Furthermore, various numerical simulations and real 3D printed objects are presented in this paper.

The paper is organized in the following manner. In Section 2 we describe the governing equation and its computational method. We provide the computational results in Section 3. In Section 4 conclusions are given.

2. Governing equation and numerical solution algorithm

To generate uniformly distributed circular pattern on surface S, we use the following temporal evolution equation [18]:

$$\frac{\partial\phi(\mathbf{x},t)}{\partial t} = \Delta\left[F'(\phi(\mathbf{x},t)) - \epsilon^2\Delta\phi(\mathbf{x},t)\right] - \alpha\left(\phi(\mathbf{x},t) - \bar{\phi}\right), \quad \mathbf{x} \in \Omega_\delta, \quad t > 0, \quad (2.1)$$

where

$$\Omega_\delta = \left\{\mathbf{y}|\mathbf{x} \in S, \mathbf{y} = \mathbf{x} + \theta\mathbf{n}(\mathbf{x}) \text{ for } |\theta| < \delta\right\}$$

is the narrow band domain embedding S and $\mathbf{n}(\mathbf{x})$ is a unit normal vector. $F(\phi) = 0.25(\phi^2 - 1)^2$, ϵ and α are positive constants, $\bar{\phi}$ is the average concentration, and $\phi(\mathbf{x},t)$ is the order parameter. Eq. (2.1) was originally developed for modeling microphase separation kinetics of block copolymer melts. It has the following total energy functional:

$$\mathcal{E}(\phi) = \int_\Omega \left(F(\phi) + \frac{\epsilon^2}{2}|\nabla\phi|^2\right)\mathrm{d}\mathbf{x} + \frac{\alpha}{2}\int_\Omega |\nabla\psi|^2\mathrm{d}\mathbf{x}, \quad (2.2)$$

where ψ satisfies $-\Delta\psi = \phi - \bar{\phi}$ [9]. Fig. 2 shows S, Ω_δ, and $\partial\Omega_\delta$.
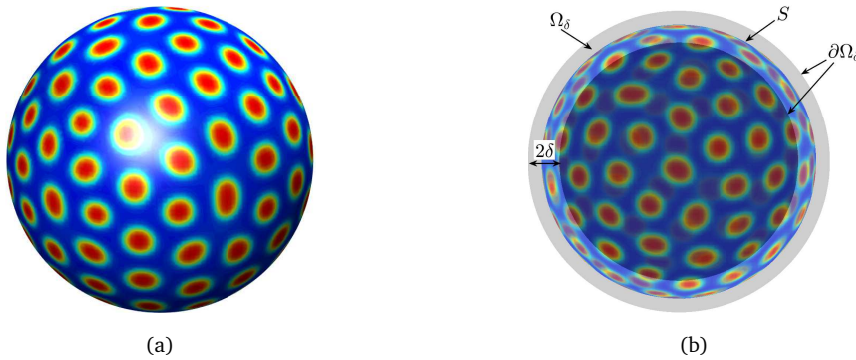

| (a) | (b) |

Figure 2: (a) Uniformly distributed circular pattern on a surface S. (b) Narrow band domain Ω_δ embedding a surface S. Here, 2δ is thickness and $\partial\Omega_\delta$ is boundary of Ω_δ.

Next we briefly review the computational solution algorithm for the nonlocal CH equation on Ω_δ [18]. We discretize Eq. (2.1) in $\Omega = (a,b) \times (c,d) \times (e,f)$ that includes Ω_δ. Let

$$h = \frac{(b-a)}{(N_x - 1)} = \frac{(d-c)}{(N_y - 1)} = \frac{(f-e)}{(N_z - 1)}$$

be the uniform mesh size, where N_x, N_y, and N_z are positive integers. Then the discrete domain is defined as

$$\Omega^h = \{\mathbf{x}_{ijk} = (x_i, y_j, z_k) : x_i = a + (i-1)h, \ y_j = c + (j-1)h, \ z_k = e + (k-1)h$$
$$\text{for} \quad 1 \le i \le N_x, \ 1 \le j \le N_y, \ 1 \le k \le N_z\}.$$

Let ϕ^n_{ijk} and μ^n_{ijk} be approximations of $\phi(x_i, y_j, z_k, n\Delta t)$ and $\mu(x_i, y_j, z_k, n\Delta t)$, respectively. We define

$$\Omega^h_\delta = \{\mathbf{x}_{ijk} : |\psi_{ijk}| < \delta|\nabla_h \psi_{ijk}|\}$$

as the discrete narrow band domain with $\delta = 1.1\sqrt{3}h$ (see Fig. 3(a)), where

$$\nabla_h \psi_{ijk} = \frac{1}{2h}(\psi_{i+1,jk} - \psi_{i-1,jk}, \psi_{i,j+1,k} - \psi_{i,j-1,k}, \psi_{ij,k+1} - \psi_{ij,k-1}).$$

Let $\partial\Omega^h_\delta = \{(x_i, y_j, z_k) : I_{ijk}|\nabla_h I_{ijk}| \ne 0\}$ be the discrete domain boundary points (see Fig. 3(a)). Here, $I_{ijk} = 0$ if $(x_i, y_j, z_k) \in \Omega^h_\delta$, and $I_{ijk} = 1$ otherwise. We use the unconditionally stable discretization of the nonlocal CH system:

$$\frac{\phi^{n+1}_{ijk} - \phi^n_{ijk}}{\Delta t} = \Delta_h \mu^{n+1}_{ijk} - \alpha \left(\phi^{n+1}_{ijk} - \bar\phi \right), \tag{2.3}$$

$$\mu^{n+1}_{ijk} = \left(\phi^{n+1}_{ijk} \right)^3 - \phi^n_{ijk} - \epsilon^2 \Delta_h \phi^{n+1}_{ijk}, \tag{2.4}$$

where

$$\Delta_h \phi_{ijk} = \frac{1}{h^2}(\phi_{i+1,jk} + \phi_{i-1,jk} + \phi_{i,j+1,k} + \phi_{i,j-1,k} + \phi_{ij,k+1} + \phi_{ij,k-1} - 6\phi_{ijk}).$$

The boundary condition on $\partial\Omega^h_\delta$ is given as

$$\phi^{n+1}_{ijk} = \phi^{n+1}(cp(\mathbf{x}_{ijk})), \quad \mu^{n+1}_{ijk} = \mu^{n+1}(cp(\mathbf{x}_{ijk})).$$

Therefore, since the boundary condition is used, we can employ the standard Laplace operator to solve Eqs. (2.3) and (2.4) instead of the Laplace-Beltrami operator [22]. Let $\mathbf{x}_{ijk} \in \partial\Omega^h_\delta$. Then

$$cp(\mathbf{x}_{ijk}) = \mathbf{x}_{ijk} - \frac{\nabla_h \psi_{ijk}}{|\nabla_h \psi_{ijk}|^2} \psi_{ijk}$$

is the closest point to the surface $\mathcal{S}$. In general, $cp(\mathbf{x}_{ijk}) \notin \partial\Omega^h_\delta$. Therefore, we calculate $\phi^n(cp(\mathbf{x}_{ijk}))$ by using trilinear interpolation (see Fig. 3(a)). We solve Eqs. (2.3) and (2.4) numerically using the Jacobi iteration method [18].

Fig. 3(b) is a schematic illustration in 2D slice: how to make narrow volume with uniformly distributed circular porous pattern as a post processing. The solid line indicates the zero-level set and dotted lines are $\partial\Omega_\delta$. The $\bullet$ indicates the point in Ω^h_δ and $\circ$ is the point in $\partial\Omega^h_\delta$. The point indicated by $\triangle$ is the rest of points in the discrete domain. At $\circ$ and $\triangle$ positions, we set $\phi = 1$. Finally, to get the 3D model with uniformly distributed circular porous pattern we make an isosurface of ϕ at a constant level.
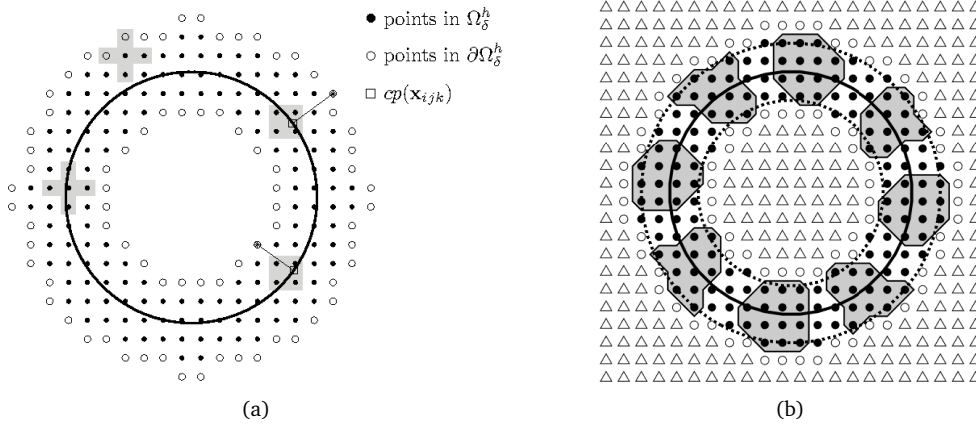
Figure 3: (a) Schematic illustration of the discrete narrow band domain Ω_δ^h. Reprinted from Jeong and Kim [18] with permission from EDP Sciences. (b) Schematic illustration of making narrow volume in the 2D discrete domain. Ω_δ^h (indicated by •) is the discrete narrow band and $\partial\Omega_\delta^h$ (indicated by ○) is its ghost points. Shaded regions in Ω_δ^h are set $\phi = -1$ and the rest of the domain (indicated by △), points in $\partial\Omega_\delta^h$ and points excluded from shaded regions in Ω_δ^h are set to $\phi = 1$.

3. Numerical experiments

In this section, we perform the test of accuracy and energy stability of our method, present numerical experiments on curved surfaces, and print the resulting 3D models. The interfacial length parameter ϵ_m is defined by $\epsilon = mh/[2\sqrt{2}\tanh^{-1}(0.9)] \approx 0.24015mh$. This means that we have an mh transition layer width approximately when $\alpha = 0$ [21]. Moreover, we determine the stopping time T when the following consecutive error e_c is less than a given tolerance level $tol = 10^{-3}$,

$$e_c = \|\phi^{n+1} - \phi^n\|_2,$$

where $\| \cdot \|_2$ is the discrete l_2-norm. We first perform the numerical investigation on basic closed surfaces such as sphere and torus. Furthermore, we present more complex surfaces such as Stanford Bunny, Armadillo, etc.

3.1. Accuracy test

Because the proposed method has first-order accuracy in time, we investigate the spatial accuracy of the method in this section. To measure the spatial accuracy, we take the numerical solution in a finer mesh as the reference solution. The domain is defined as

$$\psi(x, y, z) = \sqrt{(x - 0.5)^2 + (y - 0.5)^2 + (z - 0.5)^2} - 0.3, \tag{3.1}$$

where $(x, y, z) \in \Omega = [0, 1]^3$. An initial condition is given as follows:

$$\phi(x, y, z, 0) = -0.3 + 0.5\cos(2\pi x)\cos(2\pi y)\cos(2\pi z).$$

We fix the following parameters for all grids: $\Delta t = 10^{-6}$, $\alpha = 1000$, and $\epsilon = 0.03$. We use $N_x = N_y = N_z = M$ for $M = 33, 65, 129, 257$, hence $h = 1/32, 1/64, 1/128, 1/256$. Because $\delta = 1.1\sqrt{3}h$ depends on the value of h, we restrict the points of a coarse grid to the points only in narrow band of the finer grid when we compute the error. Let Ω_R be the set of the restricted points $\{\mathbf{x}_{ijk}\}$ of coarse grid such that $\mathbf{x}_{ijk} \in \Omega_\delta^{h/2}$. We measure the spatial accuracy at certain time $n^*\Delta t$ using $\|e^{h,n^*}\|_2$ defined as follows:

$$\|e^{h,n^*}\|_2 = \sqrt{\frac{1}{|\Omega_R|} \sum_{\mathbf{x}_{ijk}\in\Omega_R} \left(e_{ijk}^{h,n^*}\right)^2},$$

where e_{ijk}^{h,n^*} is an error between coarse and fine grids, i.e.

$$e_{ijk}^{h,n^*} = \left|\phi_{ijk}^{h,n^*} - \phi_{ijk}^{h/2,n^*}\right|, \quad \mathbf{x}_{ijk} \in \Omega_R.$$

Table 1 shows the second-order convergence rate of the spatial accuracy. We define the rate of convergence as $\log_2(\|e^{h,n^*}\|_2/\|e^{h/2,n^*}\|_2)$.

Table 1: Spatial accuracy of our method. All the values are evaluated at $t = 30\Delta t$.

$(h, h/2)$	$(1/32, 1/64)$	Rate	$(1/64, 1/128)$	Rate	$(1/128, 1/256)$
$\|e^{h,n^*}\|_2$	0.0247	1.9475	0.0064	2.0907	0.0015

3.2. Basic surfaces

We consider a spherical surface and the signed distance function to the spherical surface is defined as Eq. (3.1). We set the initial phase condition $\phi(x, y, z, 0) = -0.3 + 0.5\,\text{rand}(x, y, z)$ on the surface of a sphere. The parameters $N_x = N_y = N_z = 131$, $h = 1/(N_x - 1)$, $\Delta t = 100h$, $\alpha = 1400$, $T = 329\Delta t$, and $\epsilon = \epsilon_4$ are used. Figs. 4(a), 4(b), and 4(c) are snapshots of ϕ at $t = 5\Delta t$, $15\Delta t$, and T, whereas Figs. 4(d), 4(e), and 4(f) are isosurfaces of the final result at $\phi = 0.3$, $\phi = 0$, and $\phi = -0.3$, respectively, and Figs. 4(g), 4(h), and 4(i) are 3D printed models constructed from isosurfaces with $\phi = 0.3$, $\phi = 0$, and $\phi = -0.3$, respectively.

Furthermore, we perform the numerical investigation to see the effect of parameter α on the size and number of porous holes. In this test, we use $N_x = N_y = N_z = 181$, $h = 1/180$ and the other parameters are the same as above. In particular, we choose $\alpha = 800$, 1400, and 2200. As shown in Fig. 5, the value of α affects the size and the number of circular patterns, indeed.

Our next example is the surface of a torus. The signed distance function to the torus surface is defined as

$$\psi(x, y, z) = \left[\left(\sqrt{(x - 0.5)^2 + (y - 0.5)^2} - 0.3\right)^2 + (z - 0.5)^2\right]^{1/2} - 0.15.$$

The parameter values are the same as those of the spherical surface, except for $T = 358\Delta t$. Figs. 6(a), 6(b) and 6(c) show the phase separation on the surface of torus with initial condition $\phi(x, y, z, 0) = -0.3 + 0.5\,\mathrm{rand}(x, y, z)$ at $t = 5\Delta t$, $15\Delta t$, and T on $\Omega = [0, 1]^3$. Figs. 6(d), 6(e) and 6(f) show isosurfaces of the phase-field function of Fig. 6(c) at $\phi = 0.3$, $\phi = 0$ and $\phi = -0.3$, respectively, and Figs. 6(g), 6(h) and 6(i) are 3D printed models constructed from isosurfaces of Fig. 6(c) with $\phi = 0.3$, $\phi = 0$, and $\phi = -0.3$, respectively.
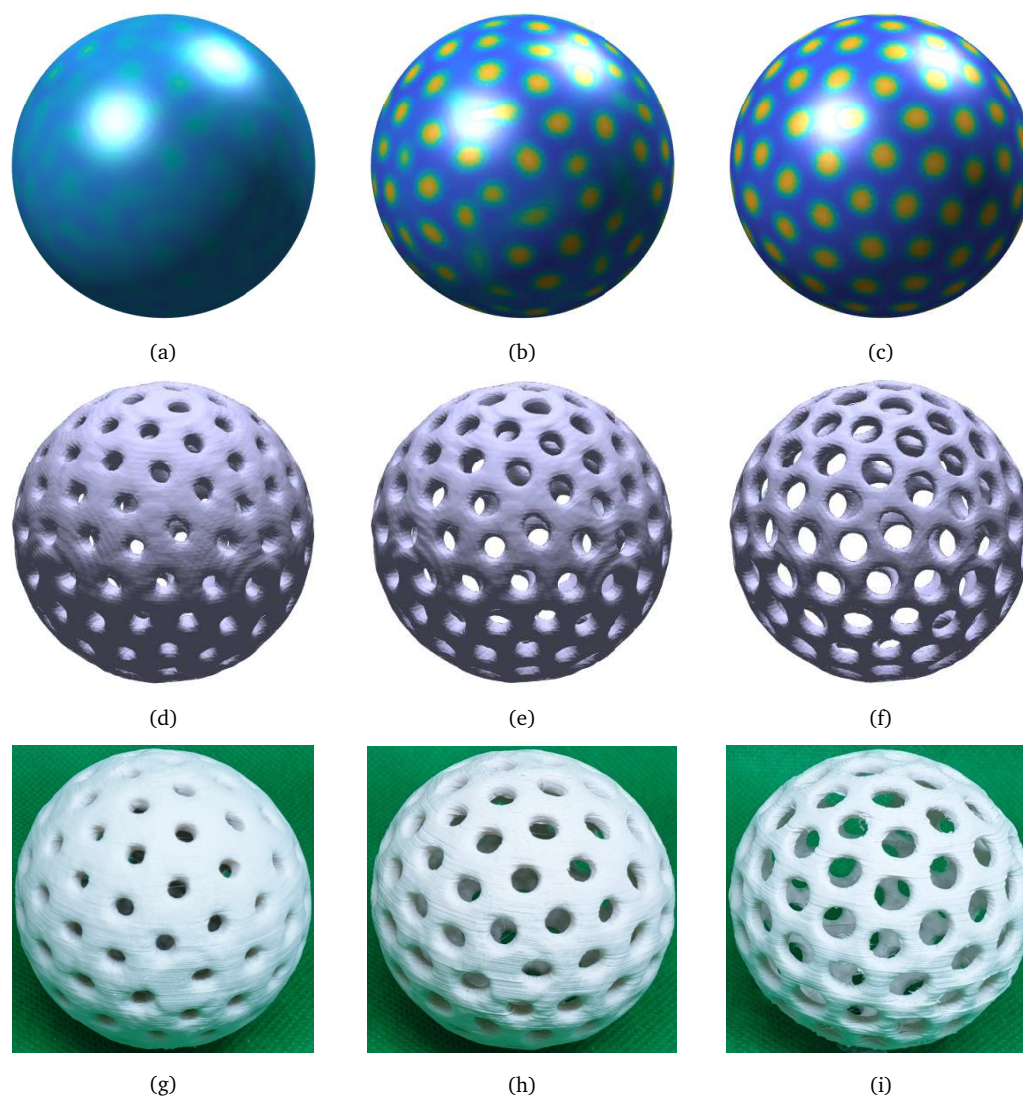

(a)   (b)   (c)

(d)   (e)   (f)

(g)   (h)   (i)

Figure 4: (a),(b), and (c) are snapshots of ϕ at $t = 5\Delta t$, $15\Delta t$, and $329\Delta t$ with an initial condition $\phi(x, y, z, 0) = -0.3 + 0.5\,\mathrm{rand}(x, y, z)$. (d),(e), and (f) are isosurfaces at $\phi = 0.3$, $\phi = 0$, and $\phi = -0.3$, respectively. (g),(h), and (i) are 3D printed models constructed from isosurfaces with $\phi = 0.3$, $\phi = 0$, and $\phi = -0.3$, respectively.
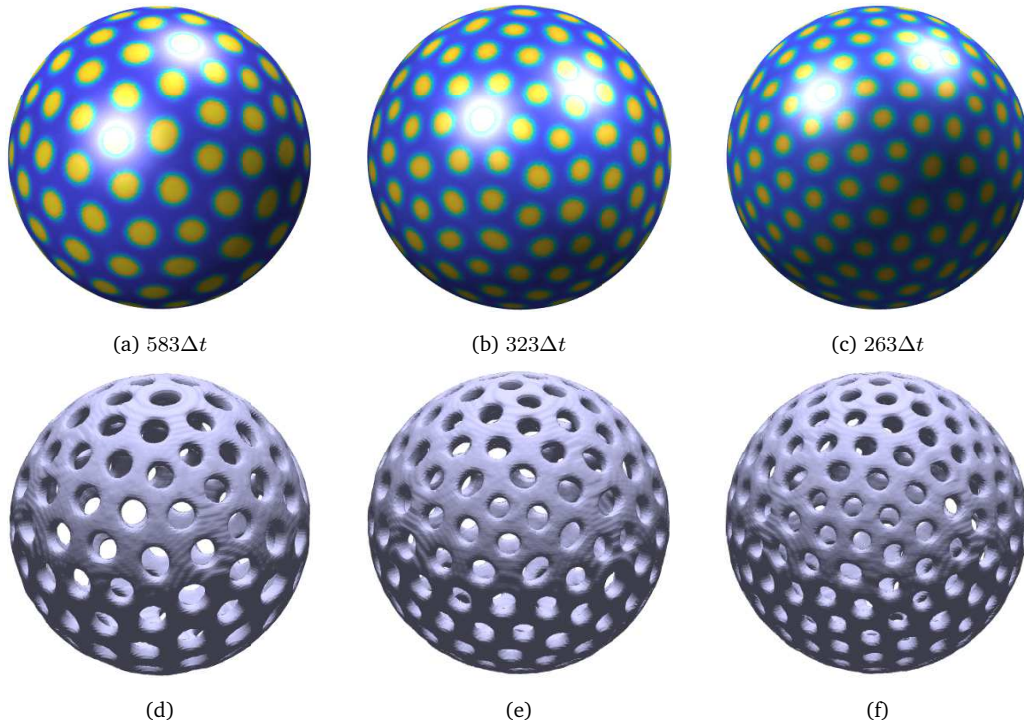
(a) $583\Delta t$ (b) $323\Delta t$ (c) $263\Delta t$

(d)   (e)   (f)

Figure 5: (a),(b), and (c) are snapshots of ϕ on sphere with $\alpha = 800, 1400,$ and 2200, respectively. The elapsed time is written under each figure. (d),(e), and (f) are isosurfaces corresponding to (a),(b), and (c), respectively.

3.3. Energy stability

In this section, we verify that our proposed method is the energy stabilized scheme by showing the energy decrease with large time step sizes. We consider the discretization of Eq. (2.2) as follows:

$$\mathcal{E}^h(\phi^n) = \sum_{\mathbf{x}_{ijk} \in \Omega_\delta^h} \left[F\left(\phi_{ijk}^n\right) + \frac{\epsilon^2}{2}\left|\nabla_h \phi_{ijk}^n\right|^2 + \frac{\alpha}{2}\left|\nabla_h \psi_{ijk}^n\right|^2 \right] h^3, \qquad (3.2)$$

where ψ^n is obtained by solving $-\Delta_h \psi^n = \phi^n - \bar{\phi}$ in the narrow band domain. Note that we set $\bar{\psi} = 0$ because the Poisson equation has the unique solution up to constant.

Fig. 7 shows the normalized discrete energy over iterations until $N_t = 100$ with various time step sizes: $\Delta t = 0.1h, 10h,$ and $1000h$. This test is conducted on sphere defined by Eq. (3.1). We use the same parameters listed above, $N_x = N_y = N_z = 131$, $h = 1/130$, $\alpha = 1400$, and $\epsilon = \epsilon_4$. As shown in Fig. 7, the discrete total energy is non-increasing over time and with large time step sizes, which implies the method is energy stable.
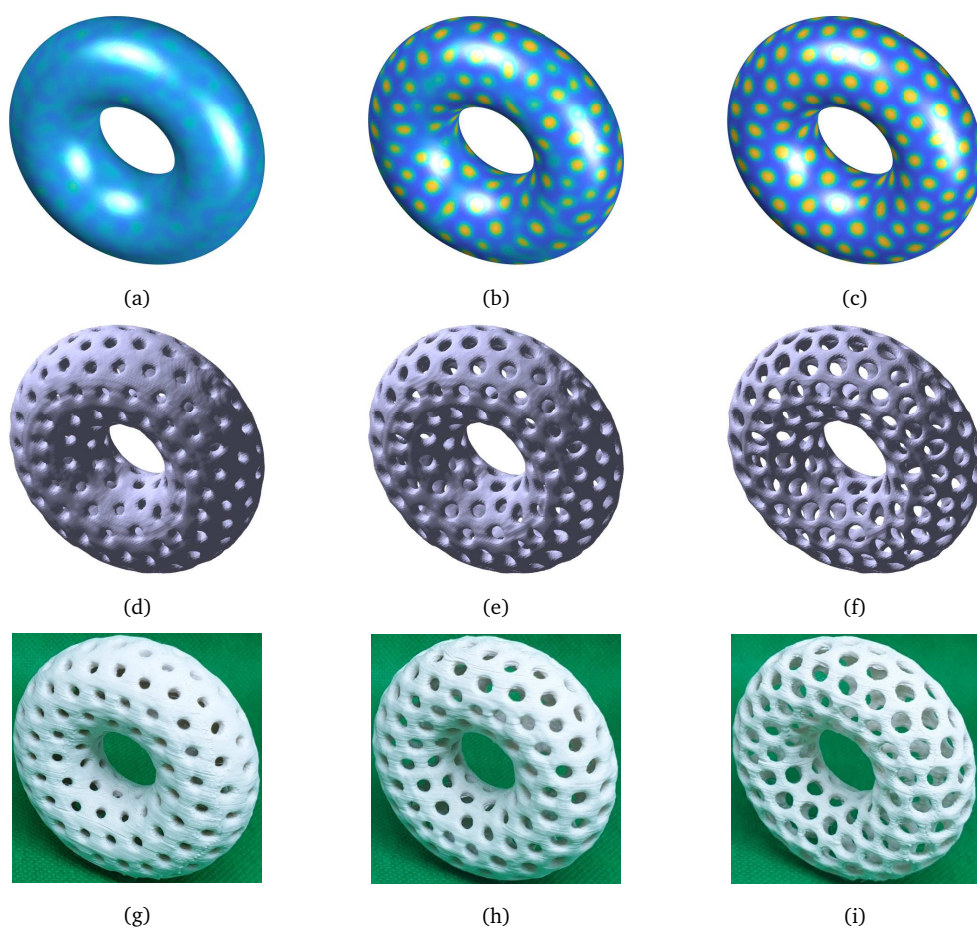
(a)   (b)   (c)

(d)   (e)   (f)

(g)   (h)   (i)

Figure 6: (a),(b), and (c) are snapshots of ϕ at $t = 5\Delta t, 15\Delta t$, and $358\Delta t$ with an initial condition $\phi(x, y, z, 0) = -0.3 + 0.5\,\mathrm{rand}(x, y, z)$. (d),(e), and (f) are isosurfaces of (c) at $\phi = 0.3, \phi = 0$, and $\phi = -0.3$, respectively. (g),(h), and (i) are 3D printed models constructed from isosurfaces of (c) with $\phi = 0.3, \phi = 0$, and $\phi = -0.3$, respectively.
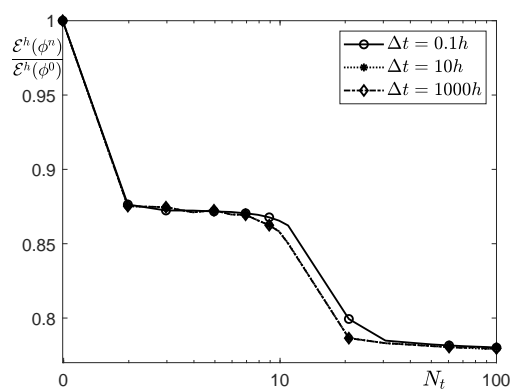

Figure 7: Normalized discrete energy dissipation over iterations until $N_t = 100$. Note that the horizontal axis is on log-scale.

3.4. Complex surfaces

We present further examples for complex surfaces with uniformly distributed circular porous patterns. Assume we have a point cloud with sufficiently dense points on a complex surface. Otherwise, we add more points. If we have triangular patches, then we can add more points by using the following procedure [19]: First, we start with a triangular patch. If the longest edge of the triangle is larger than a given tolerance, then we divide the triangle by adding the mid point. We recursively repeat this procedure until the maximum length is less than the given tolerance. Fig. 8 shows schematic illustrations of adding points.
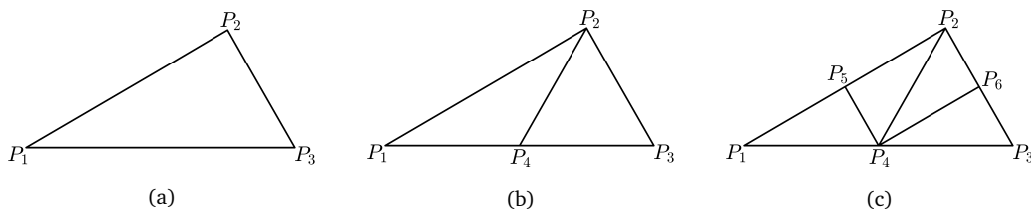

(a)   (b)   (c)

Figure 8: Schematic illustrations of adding points: (a) initial triangular patch, (b) after 1 iteration, and (c) after 2 iterations.

We use the Stanford Bunny [1] as an example for the complex surface. Figs. 9(a) and 9(b) show the original coarse point cloud and the augmented dense point cloud after applying the algorithm.

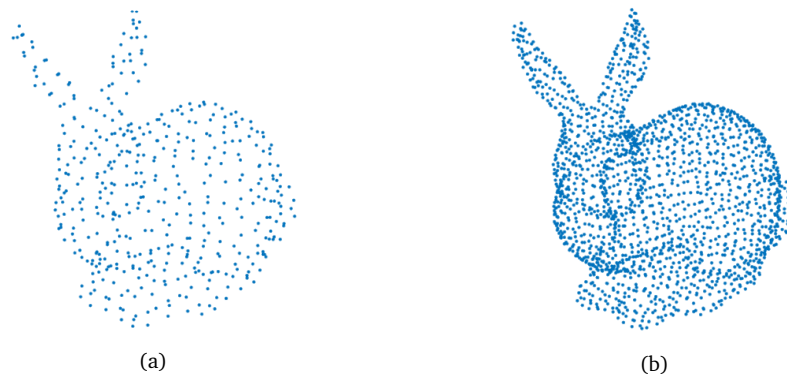(a)   (b)

Figure 9: (a) Initial point cloud. (b) Augmented point cloud.

To make a discrete signed distance function, we use an image segmentation technique using the following equation [19]:

$$\frac{\partial \psi(\mathbf{x}, t)}{\partial t} = g(\mathbf{x}) \left[-\frac{F'(\psi(\mathbf{x}, t))}{\epsilon^2} + \Delta\psi(\mathbf{x}, t) + \lambda F(\psi(\mathbf{x}, t)) \right], \qquad (3.3)$$

where λ is a parameter and $g(\mathbf{x})$ is an edge stopping function defined as the minimum Euclidean distance from point data to local mesh grid $\mathbf{x}$. More details can be found

in [19]. Once we get the discrete signed distance function, then the procedure is the same as before.

   Figs. 10(a), 10(b), and 10(c) show the phase separation on the Stanford Bunny at $t = 25\Delta t$, $t = 50\Delta t$, and $t = T$, respectively. Here, $N_x = 131$, $N_y = 129$, $N_z = 105$, $h = 1/130$, $\Delta t = 100h$, $\alpha = 2200$, $T = 239\Delta t$, and $\epsilon = \epsilon_4$ are used. Figs. 10(d), 10(e), and 10(f) show constructed isosurfaces of Fig. 10(c) to make 3D printed models, at $\phi = 0.3$, $\phi = 0$, and $\phi = -0.3$, respectively. Figs. 10(g), 10(h), and 10(i) are snapshots of 3D printed models for Figs. 10(d), 10(e), and 10(f), respectively.

   Another example of complex surface is the Stanford Armadillo from the Stanford 3D repository. Figs. 11(a), 11(b), and 11(c) show the phase separation on the Stanford Armadillo at $t = 10\Delta t$, $t = 50\Delta t$, and $t = T$, respectively. Here, we use $N_x = 130$,
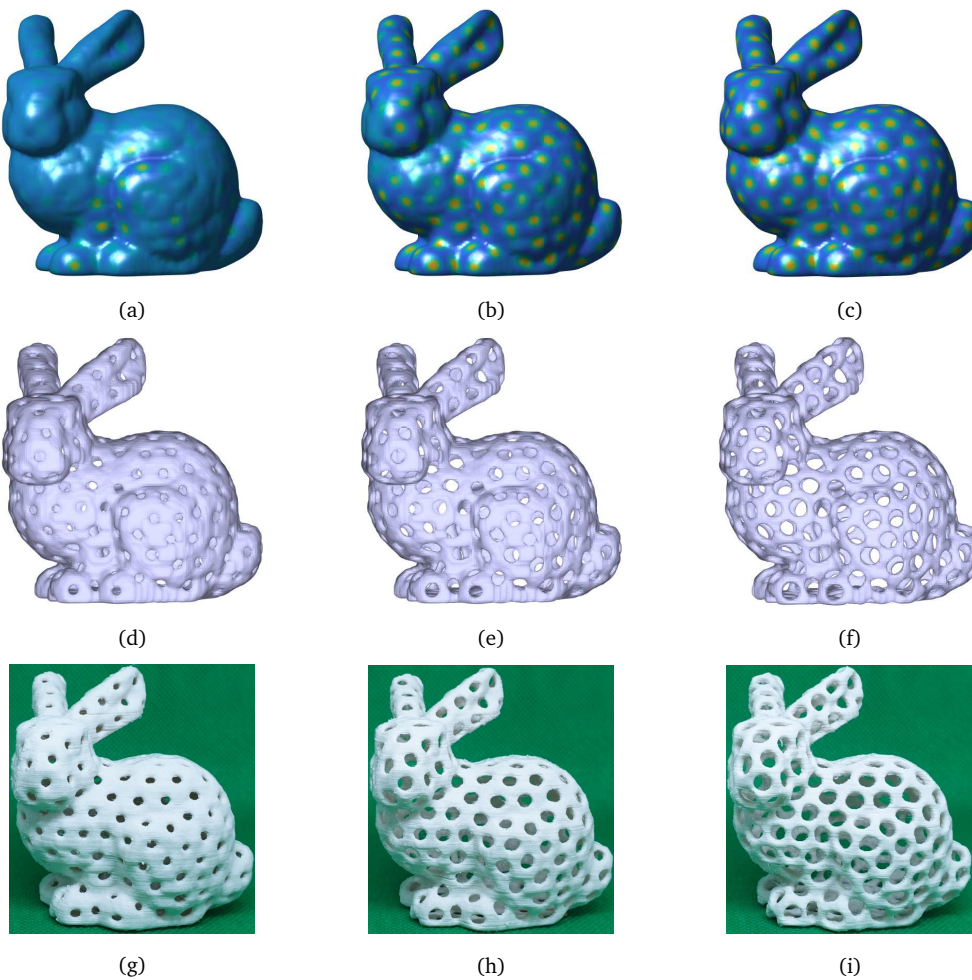

Figure 10: (a),(b), and (c) are snapshots of phase separation on the Stanford Bunny at $t = 25\Delta t, t = 50\Delta t$, and $t = 239\Delta t$, respectively. (d),(e), and (f) are isosurfaces of (c) at $\phi = 0.3, \phi = 0$, and $\phi = -0.3$, respectively. (g),(h), and (i) are snapshots of 3D printed models constructed from isosurfaces of (c) at $\phi = 0.3, \phi = 0$, and $\phi = -0.3$, respectively.

$N_y = 151$, $N_z = 119$, $h = 1/150$, $\Delta t = 100h$, $\alpha = 1800$, $T = 234\Delta t$, and $\epsilon = \epsilon_4$. Figs. 11(d), 11(e), and 11(f) show constructed isosurfaces of Fig. 11(c) to make 3D printed models, at $\phi = 0.3$, $\phi = 0$, and $\phi = -0.3$, respectively. Figs. 11(g), 11(h), and 11(i) are snapshots of 3D printed models constructed from isosurfaces for each Figs. 11(d), 11(e), and 11(f), respectively.

Fig. 12 shows several results on other complex surfaces. Note that this method is fast because it solves the partial differential equations directly on the embedded narrow band mesh; hence one can perform the conventional computations in 3D, not on surface. We measure an elapsed time that is taken to obtain a solution using our proposed method at the determined mesh size for each model. The results are listed in Table 2. In this examination, h depends on the maximum size of each mesh, however

(a)　　　　　　　　　(b)　　　　　　　　　(c)

(d)　　　　　　　　　(e)　　　　　　　　　(f)
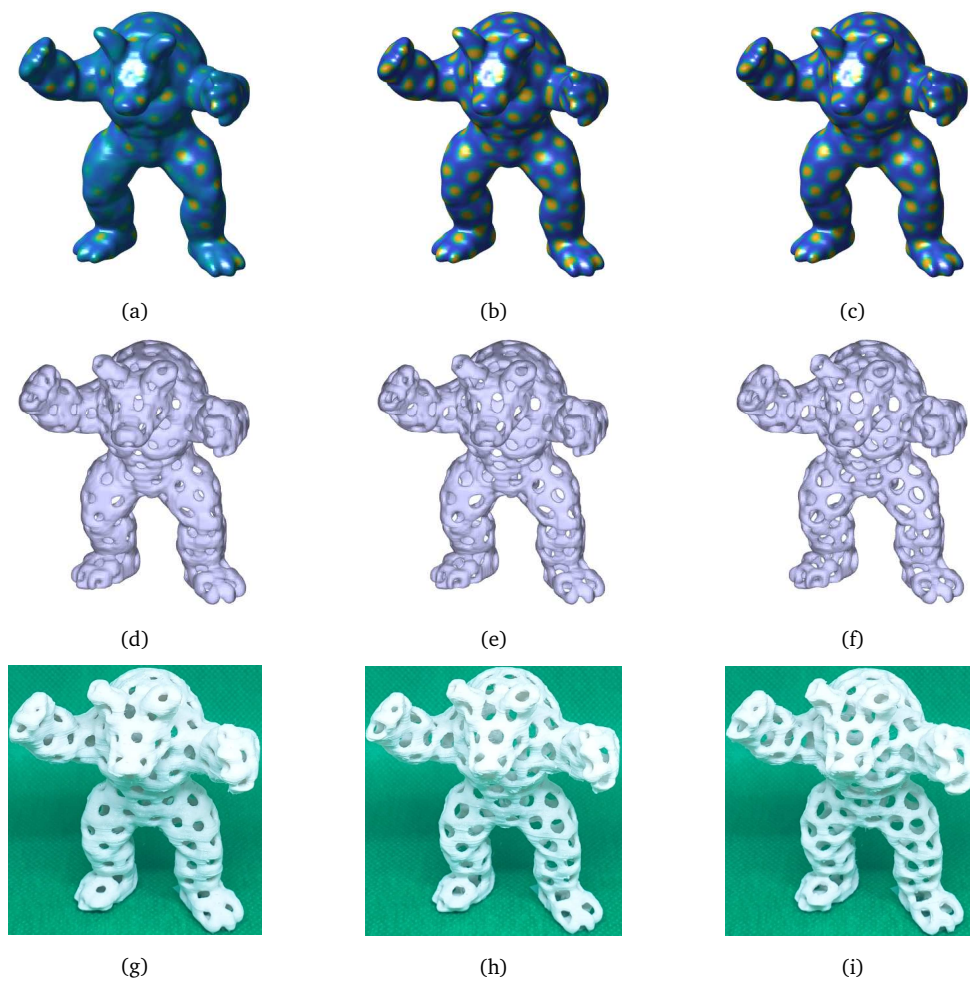
(g)　　　　　　　　　(h)　　　　　　　　　(i)

Figure 11: (a),(b), and (c) are snapshots of phase separation on the Stanford Armadillo at $t = 10\Delta t$, $t = 50\Delta t$, and $t = 234\Delta t$, respectively. (d),(e), and (f) are isosurfaces at $\phi = 0.3$, $\phi = 0$, and $\phi = -0.3$, respectively. (g),(h), and (i) are snapshots of 3D printed models constructed from isosurfaces at $\phi = 0.3$, $\phi = 0$, and $\phi = -0.3$, respectively.

Table 2: Elapsed time to find a solution for each model using the proposed method.

Model	Mesh Size (X×Y×Z)	Elapsed Time (sec)
Bunny	$131 \times 129 \times 105$	532.1
Armadillo	$130 \times 151 \times 119$	952.7
Turtle	$151 \times 97 \times 68$	639.5
Owl	$86 \times 79 \times 151$	712.9
Zebra	$48 \times 151 \times 117$	527.1

Δt is set to $100h$ and the final time T is set to $500\Delta t$. Elapsed times are all truncated from the second decimal place.

In addition, we present a post-processing to control the size of circular patterns on surfaces. For simplicity, we consider scaling using a linear function f. Fig. 13 shows 2D schematic illustrations of controlling the size of circular patterns with the linear function. The post-process was applied to the Stanford bunny described above. Figs. 14(a) and 14(b) show isosurfaces at $\phi = 0$ by adding and subtracting the linear function for z-direction, respectively. Figs. 14(c) and 14(d) show 3D printed models corresponding to Figs. 14(a) and 14(b), respectively.
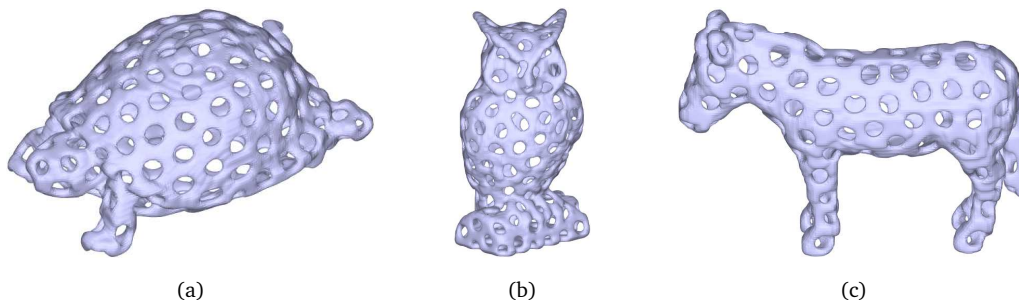

(a)   (b)   (c)

Figure 12: Each isosurface at $\phi = 0$ of (a) turtle, (b) owl, and (c) zebra, respectively.

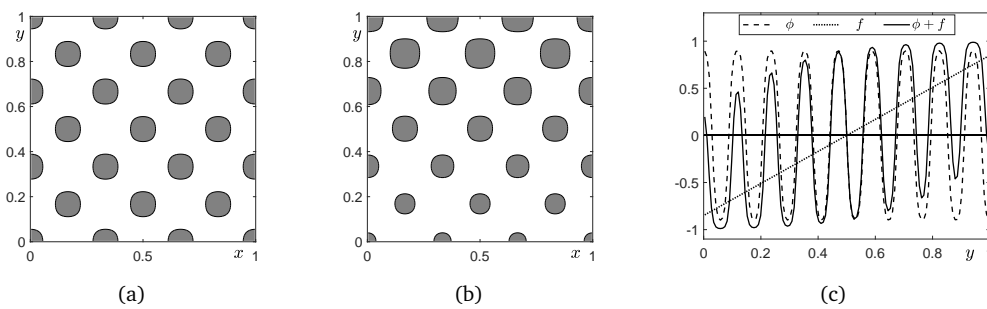(a)   (b)   (c)

Figure 13: (a) Circular patterns before scaling process. (b) Circular patterns after scaling process to $y-$direction. (c) Level curve cut from the center of circular patterns with respect to $y-$direction. $\phi + f$ is the level curve after scaling process by adding the linear function f to the phase field ϕ. Note that every circular pattern is the contour line at $\phi = 0$.
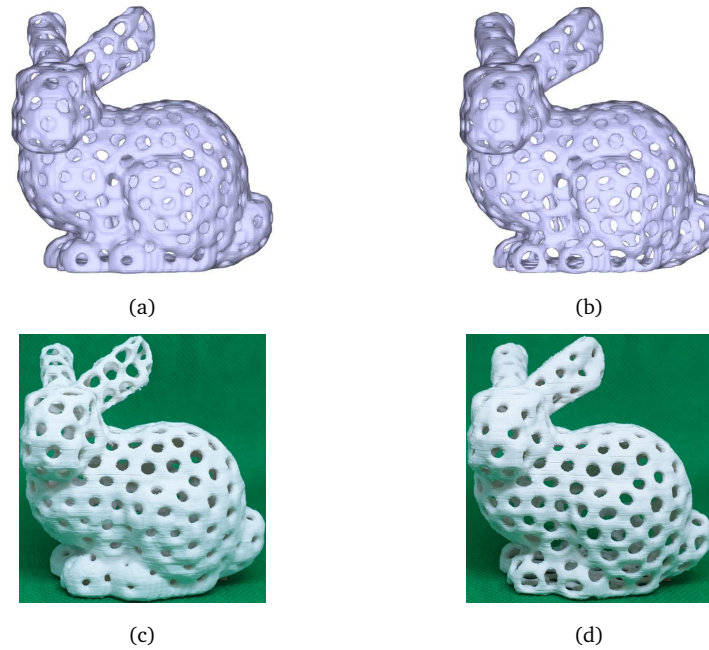
Figure 14: (a) Isosurface at $\phi = 0$ by adding the linear function for $z-$direction. (b) Isosurface at $\phi = 0$ by subtracting the linear function for $z-$direction. (c) 3D printed model with respect to (a). (d) 3D printed model with respect to (b).

4. Conclusions

In this article, we presented an algorithm for uniformly distributed circular porous pattern generation on surface in 3D printing using the nonlocal CH equation on the narrow band domain. If a surface is not represented by a level set of analytic function, then we reconstruct the surface from point cloud data and represent it as the zero-level set of discrete signed distance function. Using the proposed algorithm, we can generate uniformly distributed circular porous patterns on surface in 3D. We have verified our method has second-order accuracy in space and is the energy stabilized scheme. The computational results confirm that the proposed method is useful in designing 3D models of uniformly distributed circular porous surfaces for 3D printing applications. In future work, we will develop a numerical scheme which is of second-order in time [12, 32] for the nonlocal CH equation in the narrow band domain.

Acknowledgment

References

[1] F. Amiri, S. Ziaei-Rad, N. Valizadeh, and T. Rabczuk, *On the use of local maximum entropy approximants for Cahn–Hilliard phase-field models in 2D domains and on surfaces*, Computer Methods in Applied Mechanics and Engineering, 346 (2019), pp. 1-24.

[2] R. A. Bahr, Y. Fang, W. Su, B. Tehrani, V. Palazzi, and M. M. Tentzeris, *Novel uniquely 3D printed intricate voronoi and fractal 3D antennas*, in 2017 IEEE MTT-S International Microwave Symposium (IMS), IEEE, (2017), pp. 1583-1586.

[3] F. Buonamici, R. Furferi, L. Governi, S. Lazzeri, K. S. McGreevy, M. Servi, E. Talanti, F. Uccheddu, and Y. Volpe, *A practical methodology for computer-aided design of custom 3D printable casts for wrist fractures*, The Visual Computer, (2018), pp. 1-16.

[4] M. Burger, L. He, and C.-B. Schönlieb, *Cahn-Hilliard inpainting and a generalization for grayvalue images*, SIAM Journal on Imaging Sciences, 2 (2009), pp. 1129-1167.

[5] J. W. Cahn and J. E. Hilliard, *Free energy of a nonuniform system. I. Interfacial free energy*, The Journal of Chemical Physics, 28 (1958), pp. 258-267.

[6] S. Chaidee and K. Sugihara, *Spherical Laguerre Voronoi diagram approximation to tessellations without generators*, Graphical Models, 95 (2018), pp. 1-13.

[7] W. Chen, X. Zhang, S. Xin, Y. Xia, S. Lefebvre, and W. Wang, *Synthesis of filigrees for digital fabrication*, ACM Transactions on Graphics (TOG), 35 (2016), p. 98.

[8] L. Cherfils, H. Fakih, and A. Miranville, *A Cahn-Hilliard system with a fidelity term for color image inpainting*, Journal of Mathematical Imaging and Vision, 54 (2016), pp. 117-131.

[9] R. Choksi, M. A. Peletier, and J. F. Williams, *On the phase diagram for microphase separation of diblock copolymers: An approach via a nonlocal Cahn-Hilliard functional*, SIAM Journal on Applied Mathematics, 69 (2009), pp. 1712-1738.

[10] J. M. Church, Z. Guo, P. K. Jimack, A. Madzvamuse, K. Promislow, B. Wetton, S. M. Wise, and F. Yang, *High accuracy benchmark problems for Allen-Cahn and Cahn-Hilliard dynamics*, Communications in Computational Physics, 26 (2019), pp. 947-972.

[11] M. Corsini, P. Cignoni, and R. Scopigno, *Efficient and flexible sampling with blue noise properties of triangular meshes*, IEEE Transactions on Visualization and Computer Graphics, 18 (2012), pp. 914-924.

[12] Q. Du, L. Ju, X. Li, and Z. Qiao, *Stabilized linear semi-implicit schemes for the nonlocal Cahn-Hilliard equation*, Journal of Computational Physics, 363 (2018), pp. 39-54.

[13] M. Fernandez-Vicente, A. Escario Chust, and A. Conejero, *Low cost digital fabrication approach for thumb orthoses*, Rapid Prototyping Journal, 23 (2017), pp. 1020-1031.

[14] J. Harris and G. McShane, *Metallic stacked origami cellular materials: Additive manufacturing, properties, and modelling*, International Journal of Solids and Structures, (2019).

[15] B. S. Hosseini, S. Turek, M. Möller, and C. Palmes, *Isogeometric analysis of the Navier-Stokes-Cahn-Hilliard equations with application to incompressible two-phase flows*, Journal of Computational Physics, 348 (2017), pp. 171-194.

[16] J. Hu, S. Wang, Y. Wang, F. Li, and Z. Luo, *A lightweight methodology of 3D printed objects utilizing multi-scale porous structures*, The Visual Computer, 35 (2019), pp. 949-959.

[17] A. Jakus, N. Geisendorfer, P. Lewis, and R. Shah, *3D-printing porosity: A new approach to creating elevated porosity materials and structures*, Acta Biomaterialia, 72 (2018), pp. 94-109.

[18] D. Jeong and J. Kim, *Microphase separation patterns in diblock copolymers on curved surfaces using a nonlocal Cahn-Hilliard equation*, The European Physical Journal E, 38 (2015), p. 117.

[19] D. Jeong, Y. Li, Y. Choi, M. Yoo, D. Kang, J. Park, J. Choi, and J. Kim, *Numerical simulation of the zebra pattern formation on a three-dimensional model*, Physica A: Statistical Mechanics and its Applications, 475 (2017), pp. 106-116.

[20] D. Jeong, J. Yang, and J. Kim, *A practical and efficient numerical method for the Cahn-Hilliard equation in complex domains*, Communications in Nonlinear Science and Numerical Simulation, 73 (2019), pp. 217-228.

[21] J. Kim, *Phase-field models for multi-component fluid flows*, Communications in Computational Physics, 12 (2012), pp. 613-661.

[22] D. Lacitignola, I. Sgura, B. Bozzini, T. Dobrovolska, and I. Krastev, *Spiral waves on the sphere for an alloy electrodeposition model*, Communications in Nonlinear Science and Numerical Simulation, 79 (2019), p. 104930.

[23] X. Li, L. Ju, and X. Meng, *Convergence analysis of exponential time differencing schemes for the Cahn-Hilliard equation*, Communications in Computational Physics, 26 (2019), pp. 1510-1529.

[24] Y. Li, B. Sixou, and F. Peyrin, *Nonconvex mixed TV/Cahn-Hilliard functional for super-resolution/segmentation of 3D trabecular bone images*, Journal of Mathematical Imaging and Vision, 61 (2019), pp. 504-514.

[25] H. Lin, L. Shi, and D. Wang, *A rapid and intelligent designing technique for patient-specific and 3D-printed orthopedic cast*, 3D Printing in Medicine, 2 (2016), pp. 1-10.

[26] J. Lv, Z. Gong, Z. He, J. Yang, Y. Chen, C. Tang, Y. Liu, M. Fan, and W.-M. Lau, *3D printing of a mechanically durable superhydrophobic porous membrane for oil-water separation*, Journal of Materials Chemistry A, 5 (2017), pp. 12435-12444.

[27] L. Malomo, J. Pérez, E. Iarussi, N. Pietroni, E. Miguel, P. Cignoni, and B. Bickel, *FlexMaps: Computational design of flat flexible shells for shaping 3D objects*, in SIGGRAPH Asia 2018 Technical Papers, ACM, (2018), p. 241.

[28] Y. Mao, L. Wu, D.-M. Yan, J. Guo, C. W. Chen, and B. Chen, *Generating hybrid interior structure for 3D printing*, Computer Aided Geometric Design, 62 (2018), pp. 63-72.

[29] J. Pellerin, B. Lévy, G. Caumon, and A. Botella, *Automatic surface remeshing of 3D structural models at specified resolution: A method based on Voronoi diagrams*, Computers & Geosciences, 62 (2014), pp. 103-116.

[30] J. Pérez, B. Thomaszewski, S. Coros, B. Bickel, J. A. Canabal, R. Sumner, and M. A. Otaduy, *Design and fabrication of flexible rod meshes*, ACM Transactions on Graphics (TOG), 34 (2015), p. 138.

[31] C. Schumacher, B. Thomaszewski, and M. Gross, *Stenciling: Designing structurally-sound surfaces with decorative patterns*, in Computer Graphics Forum, vol. 35, Wiley Online Library, (2016), pp. 101-110.

[32] J. Shen and X. Yang, *Numerical approximations of Allen-Cahn and Cahn-Hilliard equations*, Discrete & Continuous Dynamical Systems - A, 28 (2010), pp. 1669-1691.

[33] Y. Song, Z. Yang, Y. Liu, and J. Deng, *Function representation based slicer for 3D print-*

ing, Computer Aided Geometric Design, 62 (2018), pp. 276-293.

[34] P. TRAN, T. D. NGO, A. GHAZLAN, AND D. HUI, *Bimaterial 3D printing and numerical analysis of bio-inspired composite structures under in-plane and transverse loadings*, Composites Part B: Engineering, 108 (2017), pp. 210-223.

[35] G. TURK, *Generating textures on arbitrary surfaces using reaction-diffusion*, in ACM SIG-GRAPH Computer Graphics, vol. 25, ACM, (1991), pp. 289-298.

[36] S. VALETTE, J. M. CHASSERY, AND R. PROST, *Generic remeshing of 3D triangular meshes with metric-dependent discrete Voronoi diagrams*, IEEE Transactions on Visualization and Computer Graphics, 14 (2008), pp. 369-381.

[37] X. WANG, X. YING, Y.-J. LIU, S.-Q. XIN, W. WANG, X. GU, W. MUELLER-WITTIG, AND Y. HE, *Intrinsic computation of centroidal Voronoi tessellation (CVT) on meshes*, Computer-Aided Design, 58 (2015), pp. 51-61.

[38] S. WISE, J. LOWENGRUB, J. KIM, K. THORNTON, P. W. VOORHEES, AND W. JOHNSON, *Quantum dot formation on a strain-patterned epitaxial thin film*, Applied Physics Letters, 87 (2005), p. 133102.

[39] X. XU AND Y. ZHAO, *Energy stable semi-implicit schemes for Allen-Cahn-Ohta-Kawasaki model in binary system*, Journal of Scientific Computing, 80 (2019), pp. 1656-1680.

[40] Y. YU, S. HUA, M. YANG, Z. FU, S. TENG, K. NIU, Q. ZHAO, AND C. YI, *Fabrication and characterization of electrospinning/3D printing bone tissue engineering scaffold*, RSC Advances, 6 (2016), pp. 110557-110565.

[41] S. ZHANG, J. GUO, H. ZHANG, X. JIA, D.-M. YAN, J. YONG, AND P. WONKA, *Capacity constrained blue-noise sampling on surfaces*, Computers & Graphics, 55 (2016), pp. 44-54.

[42] J. ZHAO, L. CHEN, AND H. WANG, *On power law scaling dynamics for time-fractional phase field models during coarsening*, Communications in Nonlinear Science and Numerical Simulation, 70 (2019), pp. 257-270.